Stroboscopic X-Ray Imaging of Vibrating Dislocations Excited by 0.58 GHz Phonons

D. Shilo and E. Zolotoyabko

Department of Materials Engineering, Technion–Israel Institute of Technology, Haifa 32000, Israel

(Received 10 March 2003; published 12 September 2003)

We report on direct imaging, by means of stroboscopic x-ray topography, of phonon-induced dislocation vibrations. X-ray images taken from $LiNbO_3$ crystals excited by 0.58 GHz surface acoustic waves, showed individual acoustic wave fronts as well as their distortions when crossing the dislocation line. The observed contrast is well explained by considering the dynamic deformation field of vibrating dislocation. Comparing simulated deformation maps and x-ray images permitted determination of the local velocities of vibrating dislocations and their viscosity coefficients. We found unexpectedly high velocity values (not far from the speed of sound) and extremely low viscosity coefficients, 2–3 orders of magnitude lower than previously measured in ductile materials.

DOI: 10.1103/PhysRevLett.91.115506 PACS numbers: 63.20.Mt, 46.40.Cd, 61.10.–i, 61.72.Ff

The motion of dislocations affects and determines a variety of mechanical, acoustic, thermal, and electrical characteristics of materials [1]. Phonon-induced dislocation vibrations significantly influence material properties related to the phonon flux, such as thermal conductivity and acoustic attenuation [2–4]. The interaction between dislocations and phonons has been extensively studied for decades [2,3,5]. Nevertheless, the established experimental methods (internal friction [4] and thermal conductivity measurements [3]) suffer from two principal disadvantages, which hamper the studies in this field. First, the existing methods provide only averaged information over a whole ensemble of dislocations with neither spatial nor temporal resolution. In other words, we are unable to resolve the interaction of phonons with individual dislocations, which is the subject of theoretical models. Second, the existing methods can be applied (and have been applied) only to ductile crystals, such as metals and alkali halides. Ductile crystals are characterized by high viscosity to dislocation motion, which results in the slowing down of dislocation movements. As will be shown below, the viscosity coefficients in brittle ceramic crystals, such as $LiNbO_3$, may be 2–3 orders of magnitude lower than in ductile crystals.

In order to overcome these difficulties and limitations we have developed a new imaging technique, high-frequency stroboscopic x-ray topography, which allows us to visualize, on the same image, the deformation fields of both individual acoustic wave fronts and vibrating dislocations. In order to visualize rapidly changing dynamic deformation fields, we conduct high-frequency stroboscopic measurements in which the acoustic wave propagation within a crystal is synchronized in time with x-ray bursts coming from a synchrotron source to the sample position. For this purpose, an acoustic signal should be phase locked to the x-ray burst periodicity, and the acoustic frequency, $f = Nf_x$, should be multiple integer of the x-ray burst frequency, f_x. Under synchronization conditions, every x-ray burst probes the same instantaneous distribution of deformations during the entire exposure [6]. As a result, the rapidly oscillating deformation field of the acoustic wave, propagating at the speed of about 4 km/s, is revealed in the diffraction images as it is frozen in time. Note, that the high-frequency surface acoustic waves (SAW) can be visualized by other methods, e.g., optically [7]. However, only stroboscopic x-ray topography allows us to simultaneously "see" the deformation fields induced by acoustic waves and extended lattice defects, such as dislocations.

First stroboscopic x-ray experiments were performed in the early 1980's with a 30 MHz SAW [8,9]. Because of the large SAW wavelength (about 100 μm) these experiments did not exhibit phonon interactions with dislocations. X-ray imaging of a 12 μm SAW has been achieved in experiments that we performed with 0.29 GHz SAW devices at the European Synchrotron Radiation Facility (ESRF, Grenoble) [6,10]. Recently, we succeeded in visualizing individual acoustic wave fronts of SAWs having 6 μm wavelength ($f = 0.58$ GHz) [11]. Some wave front distortions in the vicinity of dislocation lines were resolved and treated qualitatively in a spirit of the Granato-Lucke theory [2].

In this Letter we describe new experimental results, which were obtained at optimized contrast conditions, the latter have been found as a result of detailed analysis of x-ray focusing by SAW [12]. In this experiment we were able to stroboscopically visualize the vibrating dislocation segments in $LiNbO_3$ excited by 0.58 GHz SAWs. Comparison of x-ray diffraction images and calculated dynamic deformation fields of vibrating dislocations allowed us to obtain quantitative characteristics of individual dislocations moving in brittle ceramics.

Measurements were made at the ID19 beam line of the ESRF, utilizing the 16-bunch mode of the storage ring operation ($f_x = 5.68$ MHz). Diffraction images were taken by using (030)$LiNbO_3$ Bragg reflections and monochromatic 10 keV x rays. Images were detected by high-resolution x-ray films having spatial resolution of 3000 lines/mm. SAWs were generated by applying a 0.58 GHz electrical signal to interdigital electrodes deposited on

top of commercial (Crystal Technology, Inc.), one side polished, 3 in. diameter, *Y*-cut $LiNbO_3$ wafers. The SAW amplitude is proportional to the applied voltage, reaching about 0.1 nm at maximum sinusoidal electric signal, 7 V peak to peak.

A typical stroboscopic x-ray image, revealing the propagation of SAW and its interaction with individual dislocations, is shown in Fig. 1(a). Well-resolved acoustic wave fronts form alternating dark and light lines, which pass like a ruler through the entire image area. Besides that, the traces of three dislocation lines, almost parallel to the surface, are also visible. Dislocations are better resolved in the image shown in Fig. 1(b), which was taken for comparison from exactly the same crystal area, but after switching off the SAW. In the vicinity of the dislocation lines strong wave front deflections occur [see Fig. 1(a)] as a result of the dislocation movements under SAW excitation. By combining the dynamic deformation fields of SAWs and the vibrating dislocation we were able to simulate the local shapes of the acoustic wave fronts and to compare them with observed features in the x-ray images.

The total dynamic deformation field is expressed via the vector, $\boldsymbol{u}(x, y, z)$, which denotes atomic displacements relative to their equilibrium positions (x, y, z). In order to describe the displacement field of the SAW, $\boldsymbol{u}^S$, we used an orthogonal coordinate system (x, y, z) (see Fig. 2), with the y axis normal to the crystal surface and the z axis parallel to the SAW wave vector, $\boldsymbol{k}_s$. The Bragg scattering geometry is sensitive only to the u_y component of the displacement vector, $\boldsymbol{u}$. In the case of SAW [13]:

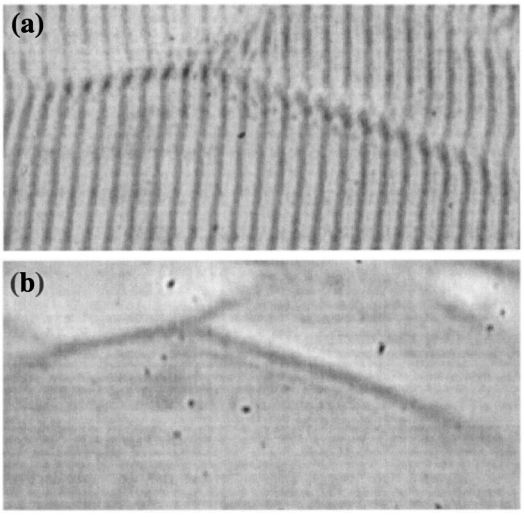

FIG. 1. (a) X-ray image taken from an $LiNbO_3$ crystal under SAW excitation, revealing pronounced distortions of acoustic wave fronts in the vicinity of dislocation lines. The spacing between nondistorted individual acoustic wave fronts (dark lines in the bottom of the image) is 6 μm; (b) x-ray image taken from the same crystal region as in (a), but with no SAW excitation.

$$u_y^S = u_{y0}(y)\cos(k_s z - \omega t), \tag{1}$$

where $\omega = 2\pi f$ is the angular frequency of the SAW.

An auxiliary coordinate system (x', y', z') is related to the vibrating dislocation, with the z' axis parallel to the dislocation line [see Fig. 2]. The x-ray topographs indicate that the dislocation lines, which strongly interact with the SAW, are almost parallel to the crystal surface and form rather small angles, $\gamma \leq 20°$, with the z axis. Hence, we chose the y' axis parallel to the y axis and the x' axis to be perpendicular to both the y' and z' axes, so that the x'–z' and x–z planes coincide.

Since screw dislocations parallel to the crystal surface result in $u_y = 0$, the deformation fields were simulated for edge dislocations with Burger's vector, $\boldsymbol{b}$, along the x' axis, i.e., perpendicular to the dislocation line (the z' axis).

The static displacement field around an edge dislocation is given in [1]:

$$u_y(x', y') = -\frac{|b|}{8\pi(1-\upsilon)}\left[(1-2\upsilon)\ln(x'^2 + y'^2) + \frac{x'^2 - y'^2}{x'^2 + y'^2}\right], \tag{2}$$

where υ is Poisson's ratio. We assume that close enough to the dislocation line ($r \leq \lambda_s$) the displacement field follows the dislocation motion [14,15]. It means that in Eq. (2) the coordinate x' should be replaced by $x' - \xi(z', t)$, where $\xi(z', t)$ describes the temporal and spatially dependent shift of the vibrating dislocation from its original position at $x' = 0$.

In the case of forced vibrations

$$\xi = \xi_0 \cos(k_d z' - \omega t + \phi), \tag{3}$$

where ξ_0 is the vibrating amplitude (real), ϕ is the phase shift relative to the phase of the SAW, and $k_d = k_s \cos\gamma$ is related to the SAW wave vector, $k_s = 2\pi/\lambda_s$. The maximum velocity of the vibrating dislocation segment,

$$V_m = \omega\xi_0 = 2\pi\frac{\xi_0}{\lambda_S}V_R, \tag{4}$$

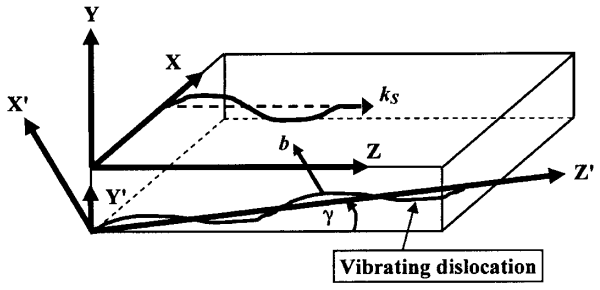

FIG. 2. Coordinate systems related to the propagating surface acoustic wave (x, y, z) and the vibrating dislocation line (x', y', z').

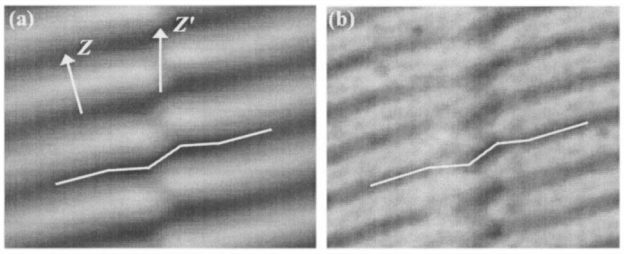

FIG. 3. X-ray image (right panel) showing wave front distortions in the vicinity of vibrating dislocation, as compared with the simulated map of the total dynamic displacement field (left panel) for $\xi_0/\lambda_S = 0.14$ and $\phi = \pi/2$. The spacing between nondistorted individual acoustic wave fronts equals 6 μm.

is determined by the ratio, ξ_0/λ_s, which manifests the strength of the dynamic phonon/dislocation interaction. Here, $V_R = \omega/k_s$ is the speed of the SAW. In the stroboscopic mode of measurement, $\omega t = 2\pi m$ (m is an integer), and the time dependence of the dynamic deformation [via Eqs. (1) and (3)] is avoided.

Simulations of the local shapes of the acoustic wave fronts by using the total dynamic displacement field, $u_y^S + \Delta u_y^d$, with $\Delta u_y^d = u_y(x' - \xi, y') - u_y(x', y')$, allowed us to reproduce all main features of the wave front distortions that appear in the collected x-ray images.

As an example, the dynamic displacement map calculated for $\xi_0/\lambda_S = 0.14$ and $\phi = \pi/2$ is shown in Fig. 3 together with one of the experimental x-ray images. It can be seen that the simulated map well describes the acoustic wave front distortions near the dislocation line. For a deeper understanding we show, in Fig. 4, two separate contributions to the dynamic deformation field. In the middle of the map, the dynamic part of the dislocation deformation field, Δu_y^d, is presented for $|x'| < \lambda_S/2$. The right-hand side and left-hand side of the map show the SAW's contribution, u_y^S, in the range of $|x'| > \lambda_S/2$. It can be seen that the term, Δu_y^d, produces a dark "zigzag"-like pattern, which is actually an image of the vibrating dislocation line, $\xi(z')$. The latter is calculated by means of Eq. (3) and indicated by a white line in Fig. 4. The angle between zigzag segments and the z' axis becomes smaller as the normalized amplitude, ξ_0/λ_S, decreases.

In the total dynamic deformation field [see Fig. 3], some of the dark segments [indicated by S1 in Fig. 4], that form the zigzag pattern, disappear since they are located exactly in the middle of the bright SAW wave fronts. Thus the observed pattern in the vicinity of the dislocation line is actually an image of the second type of zigzag segments [indicated by S2 in Fig. 4], which remain in the image.

On the other hand, for $\phi = -\pi/2$, the S2 segments of the zigzag pattern disappear, and only the S1 segments remain in the image. As a result, the simulated map (see

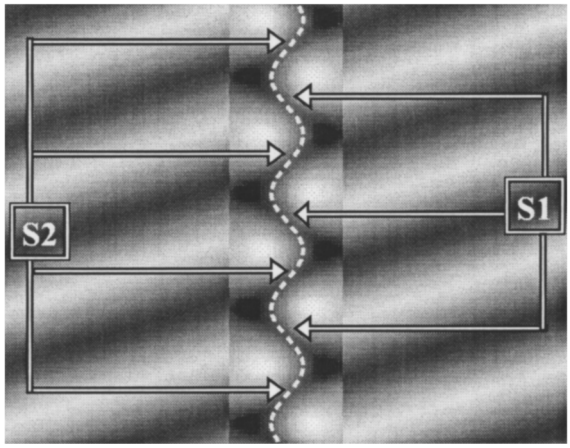

FIG. 4. Displacement fields of SAWs and a vibrating dislocation, shown separately, under the same conditions as in Fig. 3. The contribution of Δu_y^d is drawn within $|x'| < \lambda_S/2$, that of u_y^S—at $|x'| > \lambda_S/2$. The displacement field of the vibrating dislocation forms a zigzag pattern near $x' = 0$. Two types of segments that comprise the zigzag pattern are indicated by $S1$ and $S2$. Instant shape, $\xi(z')$, of the vibrating dislocation is shown by the white line.

Fig. 5) exhibits dark streaks in the vicinity of the dislocation line, which are tilted by certain angles, as compared with Fig. 3. An example of the observed x-ray image of this type is also shown in Fig. 5.

By comparing the simulated maps with experimental images we found that vibrating dislocations can be characterized by $|\phi| \cong \pi/2$ and ξ_0/λ_S ratios between 0.08 and 0.14. Substituting the ξ_0/λ_S values into Eq. (4), yields $V_m = (0.50 - 0.88) \cdot V_R \cong (0.46 - 0.81) \cdot V_T$, where $V_T \cong 1.08 \cdot V_R$ [13] is the velocity of shear bulk waves, which is considered to be the highest possible value of dislocation motion [1].

These values of dislocation velocities are 2–3 orders of magnitude higher than those previously measured in metals and alkali halides [2]. The physical reason for such high velocities under the subtle strains of about

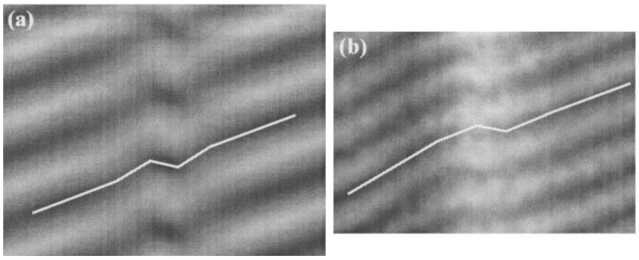

FIG. 5. X-ray image (right panel) showing wave front distortions in the vicinity of a vibrating dislocation, as compared with the simulated map of the total dynamic displacement field (left panel) for $\xi_0/\lambda_S = 0.14$ and $\phi = -\pi/2$. The spacing between nondistorted individual acoustic wave fronts equals 6 μm.

5×10^{-5} introduced by the SAW, is the low value of the coefficient of viscosity, B, to dislocation motion in brittle $LiNbO_3$.

Analysis of the crystalline structure of $LiNbO_3$ shows that the vibrating dislocations, visible in the x-ray images, do not lie along the valleys of the crystal potential, which is known as Peierls's potential [1]. Moreover, based on the kink theory [16], one can say that these dislocations are not subjected to the Peierls force, and hence their gliding is restricted only by the viscous drag of dislocation motion.

The appropriate equation of motion for dislocations not subjected to Peierls's force, is [1,2]:

$$m^* \frac{\partial^2 \xi}{\partial t^2} - T \frac{\partial^2 \xi}{\partial z'^2} + B \frac{\partial \xi}{\partial t} = \mu b \varepsilon_0 \sin(k_d z' - \omega t), \quad (5)$$

where μ is the shear modulus, $m^* \cong 0.5\ \rho b^2$ is the effective mass per unit length of the dislocation line, ρ is the material density, and $T = 0.5\ \mu b^2$ is the line tension of the dislocation which is equal to its energy per unit length. The term on the right-hand side of Eq. (5) is the SAW-induced force per unit length of the dislocation line. In fact, $\mu \varepsilon_0 \sin(k_d z' - \omega t)$ is an effective stress which can be calculated by taking derivatives, $\partial u_i^S / \partial x_j$, of the SAW's displacement field [see, e.g., Eq. (1)] and using an equality, $k_s z = k_d z'$ (i.e., $k_d = k_s \cos\gamma$).

Substituting Eq. (3) into Eq. (5), yields

$$\xi_0 = \frac{\mu \varepsilon_0 b}{B\omega} |\sin\phi|, \quad (6)$$

$$\tan\phi = \frac{B}{m * \omega[(\frac{V_T}{V_R})^2 \cos^2\gamma - 1]}. \quad (7)$$

By means of Eq. (7) it easy to explain why the phase shift of the dislocation vibration is $|\phi| \approx \pi/2$. In fact, taking $V_T/V_R \cong 1.08$ [13] and $0.94 < \cos\gamma < 1$ (for $\gamma \leq 20^\circ$), one finds that the denominator in Eq. (7) is close to zero (resonant condition), i.e., $|\phi| \approx \pi/2$. Moreover, since the exact value of V_T/V_R depends on the direction of the dislocation, the denominator in Eq. (7) can be either slightly positive or negative and, correspondingly, $\phi \cong \pi/2$ or $\phi \cong -\pi/2$.

By substituting, in Eq. (6), the obtained values of ϕ and ξ_0/λ_S as well as the experimental and material parameters: $\mu = 60$ GPa, $\varepsilon_0 = 5 \times 10^{-5}$, $b = 0.55$ nm, and $\omega = 2\pi \times 0.58$ GHz, we evaluated the viscosity coefficients, $B = (5\text{–}9) \times 10^{-6} P$. These values are 2–3 orders of magnitude lower than those measured in metals and alkali halides [5]. The results correlate well with the very low acoustic wave attenuations in $LiNbO_3$ and other brittle ceramic crystals [17], as compared with ductile materials.

In summary, by using stroboscopic x-ray topography we succeeded in visualizing the vibrating dislocations interacting with high-frequency acoustic waves (phonons). Comparison between experimental images and simulated dynamic displacement maps allowed us directly to determine the amplitudes of vibrations and the local velocities of individual dislocations. It was found that dislocations can reach nearly "relativistic" velocities ($V_m \approx V_T$) under the subtle strains introduced by SAWs. This is due to the very low viscosity to dislocation motion in $LiNbO_3$, being at least 2 orders of magnitude lower than any value measured until now in the whenever investigated materials.

Stroboscopic x-ray imaging in the GHz frequency range, as developed in this work, significantly expands our ability to investigate the phonon interaction with dislocations in single crystals, including brittle ceramics, which are beyond the scope of existing experimental techniques.

The contribution of J. Baruchel and J. Hartwig (ESRF) to this work is gratefully acknowledged. This research was supported by the Israel Science Foundation founded by the Israel Academy of Sciences and Humanities under Contract No. 389/99-11.6.

[1] F. R. N. Nabarro, *Theory of Crystal Dislocations* (Oxford University Press, New York, 1967).
[2] A. V. Granato and K. Lucke, in *Physical Acoustics*, edited by W. P. Mason (Academic Press, London, 1966), Vol. 4a.
[3] G. A. Kneezel and A. V. Granato, Phys. Rev. B **25**, 2581 (1982); G. A. Northrop, E. J. Cotts, A. C. Anderson, and J. P. Wolfe, *ibid.* **27**, 6395 (1983).
[4] F. Fanti, J. Holder, and A. V. Granato, J. Acoust. Soc. Am. **45**, 1356 (1969).
[5] V. A. Al'shitz and V. L. Indenbom, Sov. Phys. Usp. **18**, 1 (1975).
[6] E. Zolotoyabko, D. Shilo, W. Sauer, E. Pernot, and J. Baruchel, Rev. Sci. Instrum. **70**, 3341 (1999).
[7] Y. Sugawara, O. B. Wright, O. Matsuda, M. Takigahira, Y. Tanaka, S. Tamura, and V. E. Gusev, Phys. Rev. Lett. **88**, 185504 (2002).
[8] R. W. Whatmore, P. A. Goddard, B. K. Tanner, and G. F. Clark, Nature (London) **299**, 44 (1982).
[9] H. Cerva and W. Graeff, Phys. Status Solidi (a) **82**, 35 (1984).
[10] E. Zolotoyabko, D. Shilo, W. Sauer, E. Pernot, and J. Baruchel, Appl. Phys. Lett. **73**, 2278 (1998).
[11] E. Zolotoyabko, D. Shilo, and E. Lakin, Mater. Sci. Eng. A **309–310**, 23 (2001).
[12] D. Shilo and E. Zolotoyabko, J. Phys. D **36**, 122 (2003).
[13] H. Matthews, *Surface Wave Filters* (John Wiley and Sons, New York, 1977).
[14] J. D. Eshelby, Proc. R. Soc. London A **197**, 396 (1949).
[15] F. R. N. Nabarro, Proc. R. Soc. London A **209**, 278 (1951).
[16] A. Seeger, J. Phys. C **42**, C5-201 (1981).
[17] A. A. Auld, *Acoustic Fields and Waves in Solids* (Krieger Publishing Company, Malabar, 1990).